



Constrained Euler buckling: The von Kármán approximation

Jiayu Wang^{a,*}, Stéphanie Deboeuf^b, Arnaud Antkowiak, Sébastien Neukirch

^a Sorbonne Université, CNRS, Institut Jean Le Rond d'Alembert, F-75005 Paris, France

ARTICLE INFO

Keywords:

Elastic rods
Bifurcation diagram
Contact
Packing

ABSTRACT

We consider the classical problem of the buckling of a planar elastica inside a rectangular cavity. We compute the equilibrium solutions analytically in the (von Kármán) small deflection approximation. We list the different equilibrium states and their domain of validity in terms of the imposed horizontal Δ and vertical H displacements. We compute the horizontal P and the vertical F applied forces and show how they increase and scale when the compaction ratio $\sqrt{\Delta}/H$ is increased. Finally, we introduce an approximate response state, where the system adopts a periodic configuration with a noninteger number of repeated folds. This solution represents an average response of the structure and brings information on its global behavior.

1. Introduction

The buckling of elastic beams is a classical subject, especially in the planar case (Euler, 1744), (Thomson and Tait, 1883, section 611, p. 148), (Goss, 2009), (Levien, 2009, Chap. 5). Analytical solutions are known for simple (Love, 1944; Bigoni, 2012) and less simple (Djondjorov et al., 2011) cases. The global buckling behavior is nevertheless often studied numerically, and the goal is to achieve a thorough understanding of the phase diagram of the problem (Domokos, 1994) which in some cases may be cluttered (Holmes et al., 1999, Fig. 7), (Domokos and Healey, 2005, Fig. 3), (Henderson and Neukirch, 2004, Fig. 16), (Coleman and Swigon, 2004, Fig. 4). The equilibrium solutions may be computed either by direct resolution of the equilibrium equations (boundary value problem – strong form approach), finite element method (weak form approach), or minimization of the elastic energy (Charrondière et al., 2024).

The writhing and coiling of elastic rods in cavities has numerous applications. Examples comprise the helical buckling of tubings in the drilling industry (Lubinski and Althouse, 1962; Miller et al., 2015), the interaction of endoscopes and arteries in vascular surgery, the stuff box crimping in the textile industry (Hearle, 2014), DNA viral capsids (Vetter et al., 2014), spider threads in liquid drops (Elettro et al., 2016); see other examples in Judah and Givli (2024). However, the buckling of elastic beams in cavities brings the complication of inequality constraints (Villaggio, 1979) (arising from the contact condition) and their non-classical features in the bifurcation diagram (for example, corner points (Schulz and Pellegrino, 2000)). Their numerical treatment involves more sophisticated approaches, among which are linear and nonlinear complementary problems (Daviet et al., 2011), interior point

methods (Wachter and Biegler, 2006), or barrier potentials (Manning and Bulman, 2005).

The present study considers the simpler case of a planar beam buckled in a rectangular cavity. To our knowledge, this problem was first addressed by Chateau and Nguyen (1991), then Adan et al. (1994) considered the case where the constraining surface has imperfections, Domokos et al. (1997) studied pinned-pinned boundary conditions, and Pocheau and Roman (2004) unveiled the presence of multiple solutions and their self-similar aspect, as well as tilted solutions (Roman and Pocheau, 1999, 2002). The effect of the thickness of the beam was studied by Chai (1998), while Tzokova (2020) combined Abaqus FEM and experiments on beams and plates, and Katz and Givli (2015) considered the case of springy walls, see also Judah and Givli (2024). Finally, the influence of shear deformations in the section of the beam has been studied by Bosten et al. (2023) where this contact problem is used as a benchmark scenario to test finite element simulations.

Here we use what is generally called the von Kármán approximation (Woinowsky-Krieger, 1950; Eringen, 1952; Thomas, 2025). In this approximation, the moment balance is linearized, and a von Kármán-type flexural strain measure, first introduced for the buckling of elastic plates (von Kármán, 1907; Easley, 1964), is used. This model has been widely used in the literature and has shown its efficiency in computing approximate solutions for the equilibrium (Bazant and Cedolin, 2010, Section 1.9), (Neukirch et al., 2021) and dynamics (Lacarbonara and Yabuno, 2006; Pandey et al., 2014; Thomas et al., 2016) of elastic rods in the weakly nonlinear regime. It turns out that Kirchhoff himself introduced this approximated model in his book, see Kirchhoff (1876, Eq. (16), p. 441). We show in this paper that constrained Euler buckling can

* Corresponding author.

E-mail address: jiayu.wang@dalembert.upmc.fr (J. Wang).

<https://doi.org/10.1016/j.ijsolstr.2025.113279>

Received 10 December 2024; Received in revised form 22 January 2025; Accepted 6 February 2025

Available online 13 February 2025

0020-7683/© 2025 The Authors. Published by Elsevier Ltd. This is an open access article under the CC BY license (<http://creativecommons.org/licenses/by/4.0/>).

be studied and partially understood with this von-Kármán kinematics approximation; see also (Chai, 1998; Judah and Givli, 2024).

Paper contributions

In the case of small vertical (H) and horizontal (Δ) displacements:

- We present an analytical study of the Euler buckling problem with contact constraints.
- We give closed-form formulas for the vertical F and horizontal P forces and the number of folds as functions of H and Δ , and identify the scaling $FH \sim P\Delta$.
- We show that a reduced kinematic loading parameter $\sqrt{\Delta}/H$ can be used to rationalize the bifurcation curves.
- We introduce a cellular model, where the number of folds is a noninteger, that provides an all-in-one view of the response of the system.

2. Problem setup

2.1. The planar elastica

We consider an inextensible, unshearable, elastic beam buckled inside a planar, rectangular cavity. The beam has total length L , bending rigidity YI , and is horizontally clamped at both ends. The shape of the beam is studied parametrically as $(x(s), y(s))$, where s is the arc length along the beam. We introduce the angle $\theta(s)$ between the tangent to the beam and the horizontal axis e_x , see Fig. 1. As the beam is considered inextensible and unshearable, we have

$$x'(s) = \cos \theta(s), \quad y'(s) = \sin \theta(s) \quad (1)$$

where $(\cdot)' = d(\cdot)/ds$. We consider clamped boundary conditions

$$x(0) = 0 \quad y(0) = 0 \quad \theta(0) = 0 \quad (2a)$$

$$x(L) = L(1 - \Delta) \quad y(L) = 0 \quad \theta(L) = 0 \quad (2b)$$

where Δ is the (dimensionless) end-shortening, ranging from $\Delta = 0$ at buckling to $\Delta = 1$ when the two ends meet and the elastica adopts a Lemniscate-like shape (Goss, 2009). Additionally, as the beam is constrained to stay in a cavity of height H , we have the inequality constraint

$$\forall s, 0 \leq y(s) \leq H \quad (3)$$

The elastic deformation energy only involves the curvature $\kappa(s)$:

$$E_\kappa = \int_0^L \frac{1}{2} YI \kappa^2(s) ds \quad \text{where } \kappa(s) = \theta'(s) \quad (4)$$

This quadratic deformation energy is associated with the linear constitutive relation relating the internal moment $m(s)$ and the curvature

$$m(s) = YI \kappa(s) \quad (5)$$

We look for equilibrium solutions of the system, that is stationary points of this energy under constraints (2) and (3). The equilibrium condition on the internal moment reads

$$m'(s) = n_x(s) \sin \theta(s) - n_y(s) \cos \theta(s) \quad (6)$$

As we study the frictionless case, the horizontal component $n_x(s)$ of the internal force is uniform across the beam and we note $P = -n_x(s)$. The vertical component $n_y(s)$ is uniform in each free rod section and jumps every time the rod contacts the lower or the upper wall. Please also note that the moment $m(s)$ and hence the curvature $\kappa(s)$ do not experience any jump at contact points and hence are continuous along the entire rod (Bigoni, 2012). We will note F the total (vertical) force applied by the upper wall down to the rod, see Fig. 1. In this frictionless-contact case, the Hamiltonian invariant (Dichmann et al., 1996; Kehrbbaum and Maddocks, 1997)

$$I_{\text{nv}} = \frac{1}{2} YI \kappa^2(s) - P \cos \theta(s) + n_y(s) \sin \theta(s) \quad (7)$$

takes the same value in the entire system.

2.2. The von Kármán approximation

In the limit where the rod is only slightly bent, the deflection $\theta(s)$ stays small and we use the first terms in the Taylor expansion of the sin and cos functions. The equilibrium Eqs. (1), (5) and (6) simplify to

$$x'(s) = 1 - (1/2) \theta^2(s) \quad (8a)$$

$$y'(s) = \theta(s) \quad (8b)$$

$$YI \theta''(s) = -P \theta(s) - n_y(s) \quad (8c)$$

Note that the only nonlinear remaining term is in (8a), as keeping a nonlinear $\theta^2(s)$ term in (8c) would hinder the analytical approach and prevent us from expressing the solutions in terms of elementary functions. Conversely, removing the nonlinear term in (8a) would completely linearize the set of equations which would only then describe buckling modes. For more details on the von Kármán approximation and how it is obtained from dimensional reduction, please refer to Thomas et al. (2016) and Thomas (2025).

2.3. Non-dimensionalization

In this equilibrium problem, we introduce non-dimensionalized quantities

$$\hat{s} = s/L, \quad \hat{x} = x/L, \quad \hat{y} = y/L, \quad \hat{H} = H/L, \quad \hat{\theta} = \theta \quad (9a)$$

$$\hat{P} = \frac{PL^2}{YI}, \quad \hat{F} = \frac{FL^2}{YI}, \quad \hat{m} = \frac{mL}{YI}, \quad \hat{\kappa} = \kappa L \quad (9b)$$

Note that it boils down to choosing L as length unit and YI/L^2 as unit force, as can be done in most equilibrium problems of elastic rods. Please also note the non-dimensionalized version of the equations can be readily obtained by formally setting $L = 1$ and $YI = 1$ in the equations of Sections 2.1 and 2.2.

Anticipating the results of Section 4, we plot in Fig. 2 a typical bifurcation diagram where the vertical force $\hat{F} = \frac{FL^2}{YI}$ is plotted as a function of the height $\hat{H} = H/L$ of the cavity. We see that even if non-dimensionalized quantities have been used to draw the diagram, the different curves still depend on both the Atlas number n (to be defined in Section 4) and the end shortening Δ . See also Fig. 3 for the dual experiment where the end-shortening Δ is varied while keeping the height \hat{H} fixed. In this experiment, we find a dependence of the curves on both n and \hat{H} . One of the goal of the present paper is to introduce rescaled quantities on the axes that induce partial collapses of the curves of Figs. 2 and 3. Moreover, we will show that the important loading measure is $\sqrt{\Delta}/\hat{H}$.

To keep notations simple, we will drop the hats for the non-dimensionalized quantities in the remainder of the paper.

3. The arch solution

We will describe the different solution types in Section 4. They are all based on the following fundamental equilibrium solution, which we denote as the ‘Arch’ solution, see Fig. 4 and Chai (1998), Judah and Givli (2024). This solution has boundary conditions (2a) at $s = 0$. Its length is ℓ and the boundary conditions at $s = \ell$ are

$$y(\ell) = H \quad \text{and} \quad \theta(\ell) = 0 \quad (10)$$

Hence the boundary value problem to solve is system (8) with $n_y(s) \equiv -f$ together with (10) and (2a). The solution is

$$m(s) = \frac{f}{\sqrt{P}} \left(\sin \sqrt{P}s - \tan \frac{\sqrt{P}\ell}{2} \cos \sqrt{P}s \right) \quad (11a)$$

$$\theta(s) = \frac{f}{P} \left(1 - \cos \sqrt{P}s - \tan \frac{\sqrt{P}\ell}{2} \sin \sqrt{P}s \right) \quad (11b)$$

$$y(s) = \frac{f}{P\sqrt{P}} \left(\sqrt{P}s - \sin \sqrt{P}s + \tan \frac{\sqrt{P}\ell}{2} [\cos \sqrt{P}s - 1] \right) \quad (11c)$$

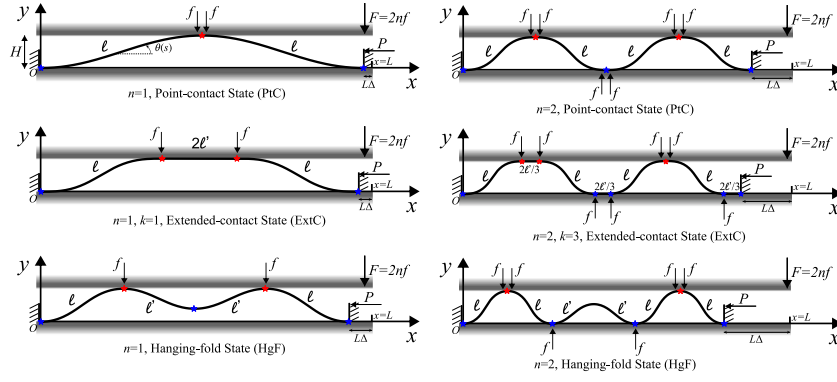


Fig. 1. Planar elastica bent in a cavity. The left end is horizontally clamped at the origin, while the right end is horizontally clamped on a block constrained to slide along the horizontal axis. The elastica has a total length L , and the angle θ is defined between the tangent to the beam and the horizontal axis. An external force is applied to the beam at $s = L$, and we note its horizontal component $-P$. Different values of the Arch number n and of the number of divisions k are shown.

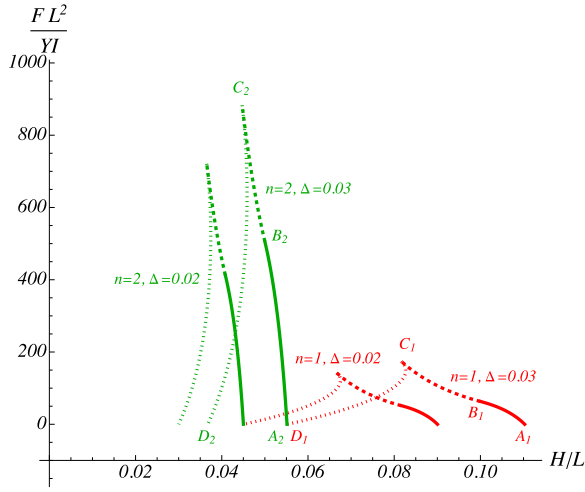


Fig. 2. The total vertical force F applied on the rod from the upper wall as a function of the height of the enclosing cavity. For $\Delta = 0.02$ and 0.03 and $n = 1$ and $n = 2$. Legend: Point-Contact state (continuous line), Extended-Contact state (dashed line, only $k = 1$), and Hanging-Fold state (dotted line).

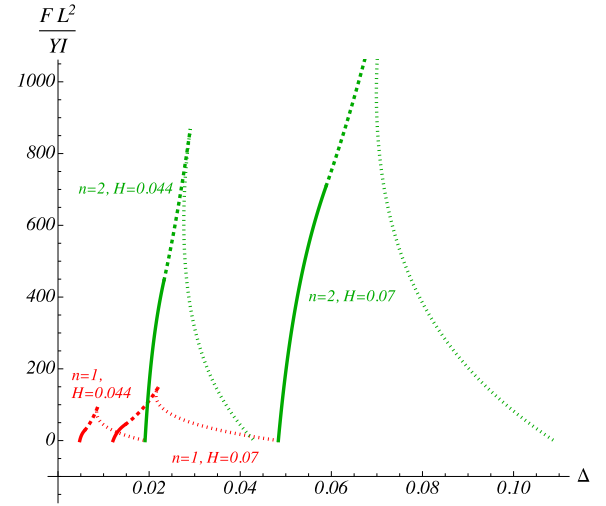


Fig. 3. The total vertical force F applied on the rod from the upper wall as a function of the end-shortening Δ . For $H = 0.044$ and 0.07 and $n = 1$ and $n = 2$. Legend: Point-Contact state (continuous line), Extended-Contact state (dashed line, only $k = 1$), and Hanging-Fold state (dotted line).

where $\pi \leq \sqrt{P}\ell \leq 2\pi$. In the following, we will need the two geometrical quantities H and $x(\ell)$, as well as the energy E_k , which are here computed as

$$H = y(\ell) = \frac{f}{P\sqrt{P}} \left(\sqrt{P}\ell - 2 \tan \frac{\sqrt{P}\ell}{2} \right) \quad (12a)$$

$$\begin{aligned} x(\ell) &= \int_0^\ell 1 - (1/2) \theta^2(s) ds \\ &= \ell - f^2 \frac{\sqrt{P}\ell [2 + \cos \sqrt{P}\ell] - 3 \sin \sqrt{P}\ell}{2P^2\sqrt{P}(\cos \sqrt{P}\ell + 1)} \end{aligned} \quad (12b)$$

$$E_k = \frac{1}{2} \int_0^\ell m^2(s) ds = \frac{f^2}{2P\sqrt{P}} \frac{\sqrt{P}\ell - \sin \sqrt{P}\ell}{1 + \cos \sqrt{P}\ell} \quad (12c)$$

Please note that, by symmetry, the moment at $s = 0$ and $s = \ell$ have the same magnitude and opposite sign

$$m(\ell) = -m(0) = \frac{f}{\sqrt{P}} \tan \frac{\sqrt{P}\ell}{2} \quad (13)$$

We emphasize that the segment length ℓ is an unknown and has to be solved for in each of the different states described in the next Section.

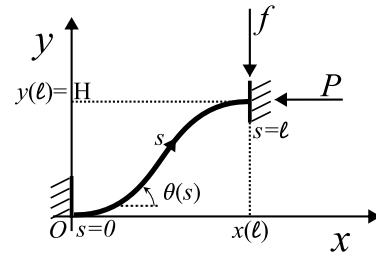


Fig. 4. The arch solution is the building block with which we compute the Point-Contact, Extended-Contact, and Hanging-Fold states presented in Section 4, as well as the cellular model presented in Section 5. This solution is in contact with both the lower and upper walls, has length ℓ , and inner force $n_x = -P$ and $n_y = -f$.

4. The different equilibrium states

In this section, we describe three different fundamental states the beam visits as either H is lowered or Δ is increased. These states have already been studied (Domokos et al., 1997; Roman and Pocheau, 2002; Chai, 1998) and we give here analytical formulas that rationalize the response of the structure and show how the horizontal and vertical loads vary as the height H and endshortening Δ are varied. The

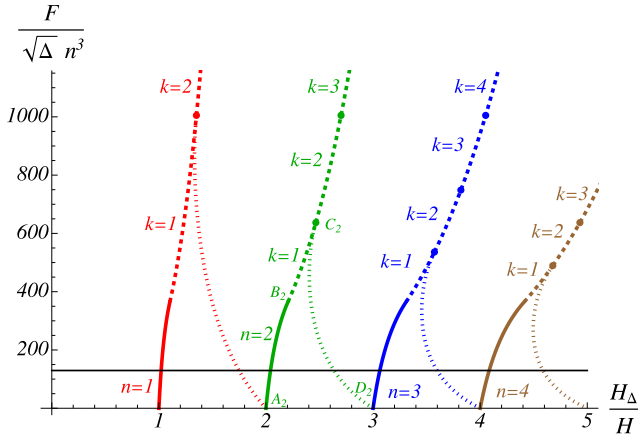


Fig. 5. Vertical force F plotted as a function of the compaction ratio H_Δ/H . This plot does not depend on the value of Δ . The threshold H_Δ is defined in Eq. (14). The black line corresponds to the continuous n model presented in Section 5. Legend: Point-Contact state (continuous line), Extended-Contact state (dashed line), and Hanging-Fold state (dotted line). We show Extended-Contact states where the flat region is divided into k pieces. For $n = 2$, we show the limit points between the different states.

elastica buckles when the horizontal force P reaches the threshold $P = 4\pi^2$ (Euler, 1744). Contact with the upper wall does not happen in this first regime where, in the present von Kármán approximation, P stays constant $P = 4\pi^2$ while H is lowered or Δ increased. Eventually, contact first happens when H and Δ are such that Bigoni (2012) and Neukirch et al. (2021)

$$H_\Delta = \frac{2}{\pi} \sqrt{\Delta} \quad (14)$$

We define the *Atlas* number n as half the number of rod segments spreading out from $y = 0$ to $y = H$ (i.e. touching both walls), such as the Arch of Section 3. In the following section, we first describe the solution for $n = 1$ and then generalize formulas for any n value. This *Atlas* number has been called the number of folds in previous works.

4.1. Point-contact states

We first describe configurations in which the elastica contacts the upper wall only at isolated point(s), see Fig. 1. We call these solutions *Point-Contact states*.

When $n = 1$, we have $\ell = 1/2$, the total force from the upper wall F takes the value $F = 2f$ and the end shortening is $\Delta = 1 - 2x(\ell)$. From the Arch solution, Eqs. (12) and (13), we have

$$H = \frac{F}{4P\sqrt{P}} \left(\sqrt{P} - 4 \tan \frac{\sqrt{P}}{4} \right) \quad (15a)$$

$$\Delta = F^2 \frac{\sqrt{P} [2 + \cos(\sqrt{P}/2)] - 6 \sin(\sqrt{P}/2)}{8P^2 \sqrt{P} [\cos(\sqrt{P}/2) + 1]} \quad (15b)$$

$$m(\ell) = -m(0) = \frac{F}{2\sqrt{P}} \tan \frac{\sqrt{P}}{4} \quad (15c)$$

This branch of solutions starts at point A_1 (see Fig. 2) when $P = 4\pi^2$, $F = 0$, $H = H_\Delta$ and ends with point B_1 when $P = 16\pi^2$, $F = 3^{-1/2} 64\pi^2 \sqrt{\Delta}$, and $H = 3^{-1/2} \sqrt{\Delta}$.

These formulas generalize directly to the case with $n \geq 1$ by setting $\ell = 1/(2n)$, $F = 2nf$, and $\Delta = 1 - 2nx(\ell)$. Using Eqs. (12) and (13) from the Arch solution, we find

$$H_u = \frac{F_u}{4P_u \sqrt{P_u}} \left(\sqrt{P_u} - 4 \tan \frac{\sqrt{P_u}}{4} \right) \quad (16a)$$

$$\Delta = F_u^2 \frac{\sqrt{P_u} [2 + \cos(\sqrt{P_u}/2)] - 6 \sin(\sqrt{P_u}/2)}{8P_u^2 \sqrt{P_u} [\cos(\sqrt{P_u}/2) + 1]} \quad (16b)$$

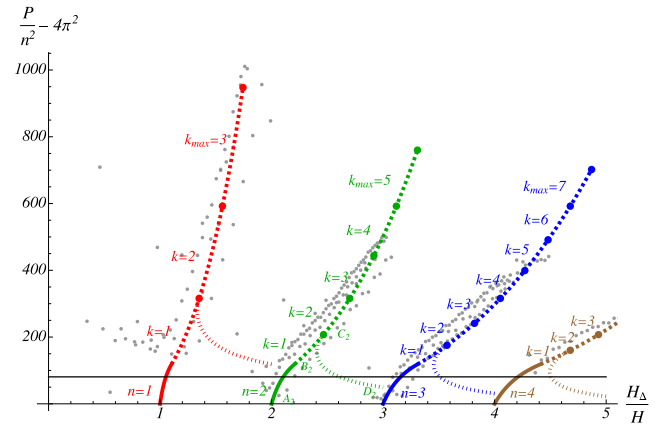


Fig. 6. Horizontal force P plotted as a function of the compaction ratio H_Δ/H . This plot does not depend on the value of Δ . The contact threshold H_Δ is defined in Eq. (14). The black line corresponds to the continuous n model presented in Section 5. Legend: Point-Contact state (continuous line), Extended-Contact state (dashed line), and Hanging-Fold state (dotted line). We show Extended-Contact states where the flat region is divided into k pieces. For $n = 2$, we show the limit points between the different states. Gray dots correspond to experimental data from Figure 5 of Deboeuf et al. (2024).

$$\frac{m(\ell)}{n} = -\frac{m(0)}{n} = \frac{F_u}{2\sqrt{P_u}} \tan \frac{\sqrt{P_u}}{4} \quad (16c)$$

with $H_u = nH$, $P_u = P/n^2$, and $F_u = F/n^3$. These branches of solutions each start at point A_n when $P_u = 4\pi^2$, $F_u = 0$, $H_u = H_\Delta$ and end at point B_n when $P_u = 16\pi^2$, $F_u = 3^{-1/2} 64\pi^2 \sqrt{\Delta}$, and $H_u = 3^{-1/2} \sqrt{\Delta}$. Using (16a) et (16b), one can write a single equation for P_u having the form $\Delta/H_u^2 = \phi(P_u)$. For $4\pi^2 \leq P_u \leq 16\pi^2$, the function $\phi(\cdot)$ is monotonously increasing, taking values from $(\pi/2)^2$ to 3, which means that, for all n , there is always a unique Point-Contact solution.

For this point-contact state, the vertical force F and the horizontal force P are plotted in plain line against the height H of the cavity for different values of the end shortening Δ in Figs. 5 and 6. We remark that, contrary to Fig. 2, the rescaling with H_Δ induces a collapse of the bifurcation curves, which now do not depend on the value of Δ . Furthermore, we show in Figs. 7 and 8 (continuous line) that, using the *Atlas* number n , the Point-Contact branches all collapse on a single curve, for any Δ and any n . We also plot in Figs. 6 and 8 the experimental data from Figure 5 of Deboeuf et al. (2024), where $\Delta < 0.16$, $0.042 \leq H \leq 0.085$, and $1 \leq n \leq 4$. In these data, friction tends to increase the measured horizontal force P which otherwise is in good agreement with the present theory.

As the first contact occurs, when $H = H_\Delta$, the vertical force F increases from $F = 0$. This is repeated for each n as we have $F = 0$ each time $nH = H_u = H_\Delta$. At this point, we compute the slope of the function $F = F(H)$ by performing a Taylor expansion of Eqs. (16a) and (16b) for H_u near H_Δ and find

$$F_u = \frac{16\pi^4}{10 - \pi^2} [H_\Delta - H_u] + \dots \quad (17)$$

The large value of the prefactor (nearly $1.2 \cdot 10^4$) shows that the vertical force steeply increases as one compresses the structure vertically.

At $P_u = 16\pi^2$, when the Point-Contact branch ends, the deflection angle at the inflexion point $s = \ell/2$ takes the value

$$\theta_{\max} = \frac{F_u}{P_u} = \frac{4}{\sqrt{3}} \sqrt{\Delta} \quad (18)$$

This maximum value yields an upper bound for Δ if we require θ_{\max} to stay small, e.g. $\theta_{\max} < 0.5$ implies $\Delta < 0.06$.

4.2. Extended-contact states

In Fig. 2, as the vertical force F is increased above point B , the beam exhibits a region where the contact with the upper (or lower)

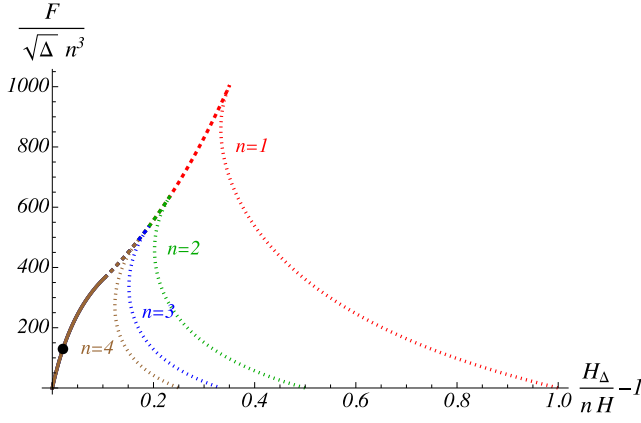


Fig. 7. Vertical force F plotted as a function of the rescaled quantity $H_\Delta/(nH) - 1$. For the Point-Contact and Extended-Contact states the plot does not depend on the Atlas number n . The entire plot does not depend on the value of Δ . The single black point at (0.02, 130) corresponds to the response of the cellular model. Legend: Point-Contact state (continuous line), Extended-Contact state (dashed line, only $k = 1$), and Hanging-Fold state (dotted line).

wall is flat; We call these solutions *Extended-Contact states*, see Fig. 1. For these solutions, both the deflection angle $\theta(s)$ and the moment $m(s)$ at the start of the flat region vanishes, and consequently the Hamiltonian invariant $I_{nv} = -P$, see Eq. (7). Additionally, as the beam is continuously flat $\theta(s) = m(s) = m'(s) = 0$, the vertical component of the internal force $n_y(s)$ has to be zero in the flat region, see Eq. (8c). Consequently there is no distributed load $n'_y(s) = 0$ coming for the wall between the touch-down and lift-off points, see Fig. 1.

When $n = 1$, we have $2\ell + 2\ell' = 1$. The value of ℓ is fixed through the condition $m(\ell) = 0$ which yields $\ell = 2\pi/\sqrt{P}$, see (13). Using the Arch solution (12) with $F = 2f$, we find

$$H = \frac{\pi F}{P\sqrt{P}} \quad (19a)$$

$$\Delta = 1 - [2x(\ell) + 2\ell'] = \frac{3\pi}{4} \frac{F^2}{P^2\sqrt{P}} \quad (19b)$$

$$m(\ell) = m(0) = 0 \quad (19c)$$

This branch of solutions starts at point B_1 (see Fig. 2) when $\ell' = 0$, $P = 16\pi^2$, $F = 3^{-1/2} 64\pi^2\sqrt{\Delta}$, and $H = 3^{-1/2}\sqrt{\Delta}$ and ends when a flat segment of the beam buckles. It has been explained that the total length $2\ell'$ of flat contact may be distributed within several sections of the beam as this would not change its energy E_κ nor its equilibrium conditions (Pocheau and Roman, 2004). We call k the number of flat sections, see Fig. 1. Buckling will happen when the horizontal force P reaches the clamp-clamp buckling threshold and one of the k flat sections buckles into a first mode shape. As each flat section has length $2\ell'/k$, the threshold is $P = 4\pi^2/(2\ell'/k)^2$. As we cannot predict the value of k , we can only give lower and upper bounds on the end of the branch, as follows. If the flat region stands in one piece, $k = 1$, the branch ends at the lower bound, point C_1 , when $\ell' = 1/6$, $P = 36\pi^2$, $F = 72\sqrt{2}\pi^2\sqrt{\Delta}$, and $H = (\sqrt{2}/3)\sqrt{\Delta}$. Alternatively, if the flat region is divided into the largest possible number of section, $k = 3$ in the present $n = 1$ case, the branch ends at the upper bound where $\ell' = 3/10$, $P = 100\pi^2$, $F = 100\sqrt{40/3}\pi^2\sqrt{\Delta}$, and $H = \sqrt{2/15}\sqrt{\Delta}$.

When $n \geq 1$, we have $2n\ell + 2\ell' = 1$, $F = 2nf$, and the condition $m(\ell) = 0$ still yields $\ell = 2\pi/\sqrt{P}$. As in Section 4.1, formulas (19) are directly generalized to

$$H_u = \frac{\pi F_u}{P_u\sqrt{P_u}} \quad (20a)$$

$$\Delta = 1 - [2nx(\ell) + 2\ell'] = \frac{3\pi}{4} \frac{F_u^2}{P_u^2\sqrt{P_u}} \quad (20b)$$

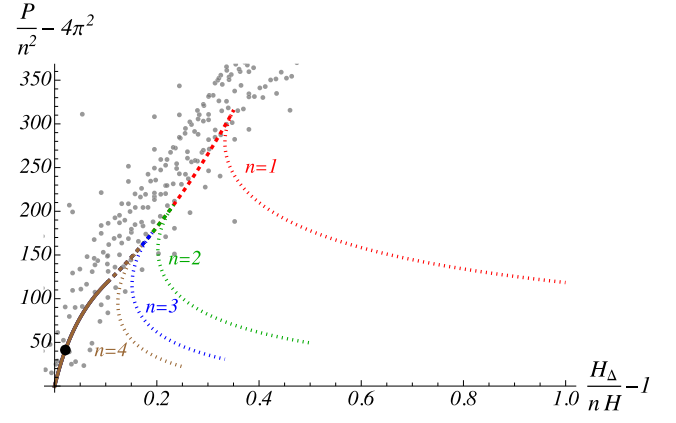


Fig. 8. Horizontal force P plotted as a function of the rescaled compaction ratio H_Δ/H . For the Point-Contact and Extended-Contact states the plot does not depend on the Atlas number n . The entire plot does not depend on the value of Δ . The single black point at (0.02, 41) corresponds to the response of the cellular model. Legend: Point-Contact state (continuous line), Extended-Contact state (dashed line, only $k = 1$), and Hanging-Fold state (dotted line). Gray dots correspond to experimental data from Figure 5 of Deboeuf et al. (2024).

$$m(\ell) = m(0) = 0 \quad (20c)$$

This rescaling of the Extended-Contact solution for any n and any Δ is illustrated in Figs. 7 and 8 (dashed line) where we see that all the ($n \geq 1$) Extended-Contact solution branches collapse. This branch of solutions starts at point B_n when $\ell' = 0$, $P_u = 16\pi^2$, $F_u = 3^{-1/2} 64\pi^2\sqrt{\Delta}$, and $H_u = 3^{-1/2}\sqrt{\Delta}$ and ends when the flat region buckles. As the flat region could be divided into k pieces (with k from $k = 1$ to $k = 2n + 1$), the branch of solutions ends when one of the k flat segment buckles, that is $P = 4\pi^2/(2\ell'/k)^2$ as explained above, and we have

$$\ell' = k/(4n + 2k) \text{ and } \ell = 1/(2n + k) \quad (21a)$$

$$P_u = 4\pi^2 \left(\frac{2n + k}{n} \right)^2 \quad (21b)$$

$$F_u = 8\pi^2 \sqrt{\Delta} \sqrt{2/3} \left(\frac{2n + k}{n} \right)^{5/2} \quad (21c)$$

$$H_u = \sqrt{\Delta} \sqrt{2/3} \sqrt{\frac{n}{2n + k}} \quad (21d)$$

which means that for large n and with a flat region divided into a maximum number of pieces ($k = 2n + 1$) the vertical force can take values up to $F \simeq 2000n^3\sqrt{\Delta} \simeq 140\Delta^2/H^3$, and the horizontal force values up to $P \simeq 600n^2 \simeq 100\Delta/H^2$.

4.3. Hanging-fold states

Along the Extended-Contact solution branch, when the flat region is in one piece, $k = 1$, a new branch bifurcates as the compression force P exceeds the buckling threshold given in (21b). A hanging fold is created, replacing the flat region, see Fig. 1. We call these configurations *Hanging-Fold states*. Please note that a configuration having a fold and a flat region is not possible, as it would imply two different values of the Hamiltonian invariant I_{nv} : the invariant value for solutions with a flat region is $I_{nv} = -P$ and the invariant value for solutions with a fold is $I_{nv} = -P + (1/2)\kappa^2(\ell) > -P$.

When $n = 1$, we have $2\ell + 2\ell' = 1$ where the value of ℓ' is fixed by Eq. (A.1) in Appendix A. We have $F = 2f$ and $\Delta = 1 - 2[x(\ell) + x(\ell')]$ where $x(\ell)$ is given by Eq. (12b) and $x(\ell')$ by Eqs. (A.2) and (A.3) in Appendix A. Further using (12a) for the height H , we find

$$H = \frac{F}{2P\sqrt{P}} \left(\sqrt{P}\ell - 2 \tan \frac{\sqrt{P}\ell}{2} \right) \quad (22a)$$

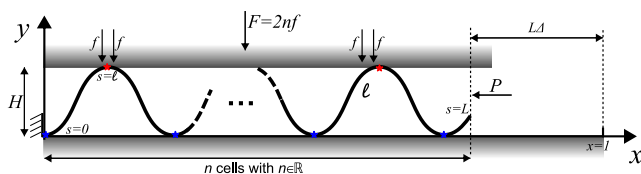


Fig. 9. In the cellular model, the system is the repetition of the Arch solution with $L = 2n\ell$. As the Atlas number n takes non-integer values, the boundary condition at $s = L$ is unsatisfied. The importance of this defect decreases as n gets large and is in fact already minor for small n values.

$$\Delta = F^2 \left\{ \frac{\sqrt{P}\ell \left[2 + \cos \sqrt{P}\ell \right] - 3 \sin \sqrt{P}\ell}{4P^2 \sqrt{P} (\cos \sqrt{P}\ell + 1)} + \frac{1/2 - \ell}{8P^2} \frac{1 - \cos \sqrt{P}\ell}{1 + \cos \sqrt{P}\ell} \right\} \quad (22b)$$

$$P = \left(\frac{\pi}{1/2 - \ell} \right)^2 \quad (22c)$$

This branch starts at point C_1 (see Fig. 2) when $\ell = 1/3$, $\ell' = 1/6$, $P = 36\pi^2$, $F = 72\sqrt{2}\pi^2\sqrt{\Delta}$, and $H = (\sqrt{2}/3)\sqrt{\Delta}$ and ends at point D_1 when $\ell = 1/4$, $\ell' = 1/4$, $P = 16\pi^2$, $F = 0$, and $H = H_\Lambda/2$.

When $n \geq 1$, we have $2n\ell' + 2\ell'' = 1$ where the value of ℓ' is still given by Eq. (A.1) in Appendix A. We have $F = 2nf$ and $\Delta = 1 - 2 \lfloor nx(\ell') + x(\ell'') \rfloor$ where $x(\ell')$ is given by Eq. (12b) and $x(\ell'')$ by Eqs. (A.2) and (A.3) in Appendix A. As in Sections 4.1 and 4.2, we use $H_u = nH$, $P_u = P/n^2$, and $F_u = F/n^3$ to write the generalization of Eqs. (22) to any $n \geq 1$ value

$$H_u = \frac{F_u}{2P_u \sqrt{P_u}} \left(\sqrt{P_u} \ell_u - 2 \tan \frac{\sqrt{P_u} \ell_u}{2} \right) \quad (23a)$$

$$\Delta = F_u^2 \left\{ \frac{\sqrt{P_u} \ell_u [2 + \cos \sqrt{P_u} \ell_u] - 3 \sin \sqrt{P_u} \ell_u}{4 P_u^2 \sqrt{P_u} (\cos \sqrt{P_u} \ell_u + 1)} + \frac{1/2 - \ell_u}{8 P^2} \frac{1 - \cos \sqrt{P_u} \ell_u}{1 + \cos \sqrt{P_u} \ell_u} \right\} \quad (23b)$$

$$P_u = \frac{1}{n^2} \left(\frac{\pi}{1/2 - \ell_u} \right)^2 \quad (23c)$$

where we have introduced $\ell_u = n\ell$. The explicit presence of the Atlas number n in Eq. (23c) implies that, contrary to what was found in Sections 4.1 and 4.2, there is no for-all- n collapse of the solution branches for the Hanging-Fold states, as can be seen in Figs. 7 and 8. The $n \geq 1$ branches start when $\ell = 1/(1+2n)$, $\ell' = 1/(2+4n)$, $P = 4\pi^2(1+2n)^2$, $F = 8\pi^2\sqrt{4}/\sqrt{2/3}(1+2n)^{5/2}\sqrt{n}$, and $H = \sqrt{24}/\sqrt{3n(1+2n)}$ and ends when $\ell = \ell' = 1/(2+2n)$, $P = 4\pi^2(1+n)^2$, $F = 0$, and $H = H_A/(1+n)$.

We recall that the description of the sequence of the different states we have made in this Section 4 holds both when H is constant and Δ increased or when Δ is constant and H decreased: The important quantity defining the state of the system is the compaction ratio H_Λ/H .

5. The continuous n approximation: The cellular model

As the compaction ratio $H_{\Delta}/H = 2\sqrt{\Delta}/(\pi H)$ is increased, the beam repeatedly visits the Point-Contact state with an increasing Atlas number n . When n becomes large, the precise boundary conditions at the rod extremities become less important, that is the integer character of n is no longer critical and one could approximate the system's response with a model where n is a non-integer quantity, see Fig. 9. We look for the equilibrium of such a cellular system by minimizing the total potential energy

$$E_{\text{tot}} = 2nE_c + 2nx(\ell)P + y(\ell)F \quad (24)$$

where we work in the dead loading case (i.e. for prescribed P and F) as it yields simpler calculations than the (equivalent) rigid loading case (i.e. for prescribed Δ and H). We use Eqs. (12) with $2n\ell = 1$ and $F = 2nf$, and find

$$E_{\text{tot}}(z) = P + \frac{F^2}{2P^2} z [\mu_x(z) - \mu_y(z) + \mu_z(z)] \quad (25a)$$

$$\text{with } \mu_k(z) = \frac{z - \sin z}{1 + \cos z} \quad (25b)$$

$$\mu_x(z) = \frac{z(2 + \cos z) - 3 \sin z}{1 + \cos z} \quad (25c)$$

$$\mu_y(z) = 2z - 4 \frac{\sin z}{1 + \cos z} \quad (25d)$$

with $z = \sqrt{P} \ell$. The minimum is reached for $z = z_e$ such that $z_e = \tan z_e$, that is $z_e \simeq 4.5$. For this solution, we have $\mu_e = \mu_x(z_e) = \mu_y(z_e) = 2\mu_v(z_e) \simeq 14$ and

$$P = \frac{z_e \mu_e}{2} \frac{\Delta}{H^2} \simeq 31 \frac{\Delta}{H^2} \quad (26a)$$

$$F = \frac{z_e \mu_e}{2} \frac{\Delta^2}{H^3} \simeq 31 \frac{\Delta^2}{H^3} \quad (26b)$$

$$n = \sqrt{\frac{\mu_e}{8z_e}} \frac{\sqrt{A}}{H} \simeq 0.62 \frac{\sqrt{A}}{H} \quad (26c)$$

$$2nE_{\kappa} = \frac{z_e \mu_e}{4} \frac{\Delta^2}{H^2} \simeq 16 \frac{\Delta^2}{H^2} \quad (26d)$$

Eq. (26c) is to be compared to Eq. (2.19) of Tzokova (2020) PhD dissertation, which also introduced a continuous approach based on the vertical force F peaks. The total curvature energy of the cellular system, $2nE_k$, is plotted in Fig. 10 and compared to the total curvature energy of the different states introduced in Section 4. In this Fig. 10, we see that the cellular model is approximately a convexification of the energy of the ‘exact’ system: Non-integer n values of the cellular model appear as approximate phase transitions between the integer- n states of the ‘exact’ system.

Using the scalings introduced in Section 4, we can rewrite these quantities as

$$P_u = \frac{P}{n^2} = 4z_e^2 \simeq 81 \text{ and } F_u = \frac{F}{n^3} = \frac{8\sqrt{2}z_e^{5/2}}{\sqrt{\mu_e}} \sqrt{\Delta} \simeq 130\sqrt{\Delta} \quad (27)$$

(See [Appendix B](#) for the different other ways to express these quantities). These quantities are plotted in [Figs. 5, 6, 7, 8, and 10](#) as black lines. Another important quantity is the maximum value of the deflection angle θ which happens at the inflection point $s = \ell/2$. In this continuous n model, we have

$$\theta_{\max} = \frac{\cos(z_e/2) - 1}{\cos(z_g/2)} \frac{F_u}{P_u} \simeq 1.3 \frac{F_u}{P_u} \simeq 2.1 \sqrt{A} \quad (28)$$

which near the value found for the Point-Contact state, see Eq. (18), and therefore yields the same limit $\Delta < 0.06$ to stay in the small angle, $\theta_{\max} < 0.5$, regime.

In Fig. 11 we plot the vertical force F as a function of the horizontal force P , with properly rescaled axes. As explained earlier, for Point-Contact and Extended-Contact states this (P, F) diagram does not depend on the values of Δ or n . Moreover, we see that the relation is almost linear, with a slope value approximately given by the cellular model: $\frac{130}{81-4\pi^2} \simeq 3.1$. Additionally, we plot the numerical results of the fully nonlinear system (1)–(6) for Point-Contact and Extended-Contact solutions to measure how much the nonlinearities cause a deviation from the virtually linear (P, F) relation, see gray dots in Fig. 11 and Wang et al. (2025). This linear relation implies that

$$F H \sim P \Delta \quad (29)$$

which means that the work done by the horizontal and vertical loads are comparable.

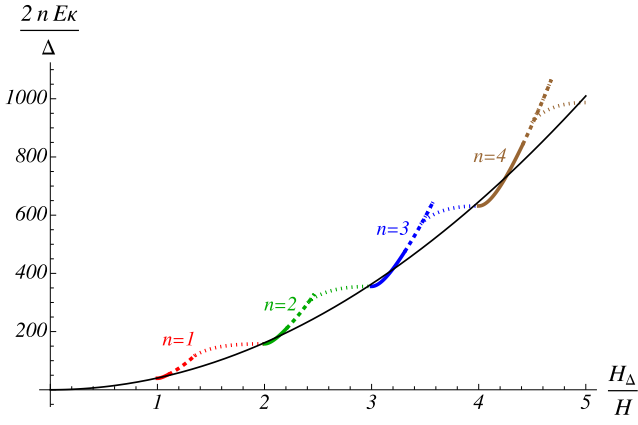


Fig. 10. Curvature energy of the beam as a function of the compaction ratio H_Δ/H . Point-Contact states (continuous line), Extended-Contact states (dashed line, only $k = 1$), and Hanging-Fold states (dotted line) are shown for $n = 1$ to $n = 4$. The black line corresponds to the continuous- n model, Eq. (26d), and is approximately a convexification of the energy of the system.

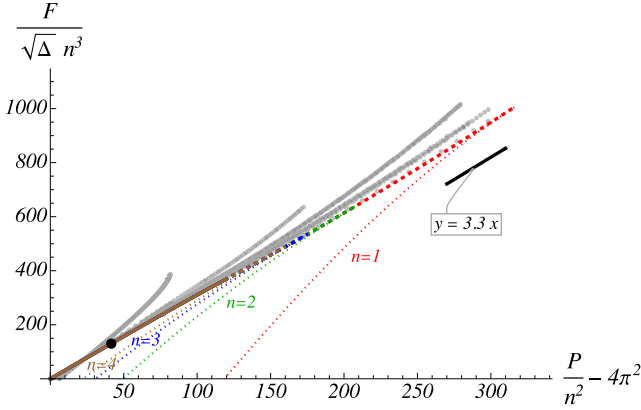


Fig. 11. Evolution of the horizontal P and the vertical F forces as H is decreased or Δ is increased. Point-Contact state (continuous line), Extended-Contact state (dashed line, only $k = 1$), and Hanging-Fold state (dotted line). For the Point-Contact and Extended-Contact states the plot does not depend on the Atlas number n . The single black point at (41, 130) corresponds to the response of the cellular model. The black line, with slope 3.3, is drawn as a guide to the eye to show the roughly linear behavior of the Point-Contact and Extended-Contact states. Gray dots correspond to numerical solutions of the nonlinear system (1)–(6) where only Point-Contact and Extended-Contact states are shown, a total of 1298 points with $H \in (0.02, 0.15)$ and $\Delta \in (0.006, 0.4)$.

6. Global phase diagram

In a typical experiment, one imposes the value of Δ and H and observes the state of the system. In Fig. 12, we plot the limit of the ranges of the existence of the different states for $n = 1$ and $n = 2$ and see that a clear arrangement materializes, linked to the compaction ratio H_Δ/H (for simplicity reasons, we only consider Extended-Contact states with their flat region in $k = 1$ piece). Nevertheless, as shown in Fig. 13, where nH is plotted as a function of $\sqrt{\Delta}$, this arrangement is not conserved as n is increased: point A_{n+1} (of slope $\frac{2}{\pi} \frac{n}{n+1}$) moves relatively to point C_n (of slope $\sqrt{\frac{2n}{2n+1}}/\sqrt{3}$) and crosses it at $n \simeq 7.1$. At a larger n value ($n \simeq 9.7$), the same point A_{n+1} even crosses point B_n (of slope $1/\sqrt{3}$). And at $n \simeq 16.8$ it is point A_{n+2} that crosses C_n . Eventually, for any fixed integer j , when $n \rightarrow \infty$ the arrangement is such that A_{n+j} is reached before B_n (in terms of compaction ratio H_Δ/H values). In contrast, the points B_n and C_n keep their relative positioning: $B_n > C_n > B_{n+1} > C_{n+1} > \dots > B_{n+j} > C_{n+j}$, for any n and j . Overall, we conclude that for $n < 8$ (and under the assumption $k = 1$),

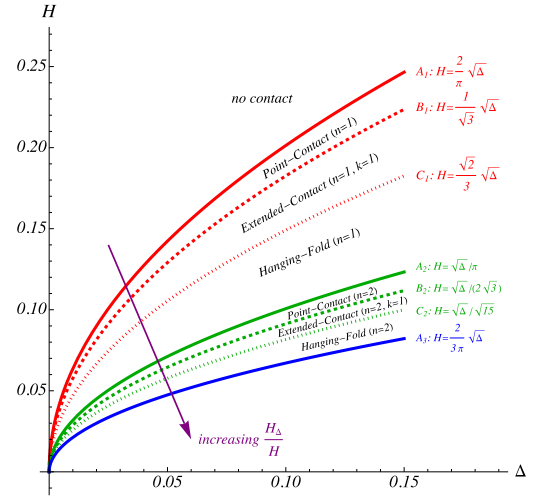


Fig. 12. An attempt to draw a global bifurcation diagram for the Constrained Euler Buckling problem. Here, we give the state of the system for given values of H and Δ , and for Atlas numbers $n = 1$ and $n = 2$. A clear arrangement of the different solutions appears, but this arrangement does not hold for any n , as is shown in Fig. 13.

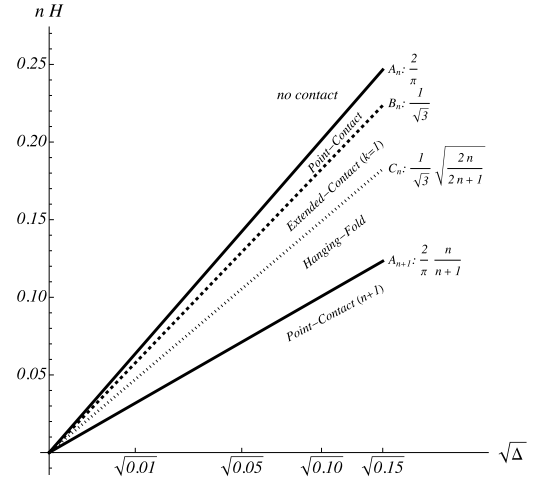


Fig. 13. The relative positioning of the curves in Fig. 12 does not hold for any n . The curves B_n and C_n keep their relative positioning, but the curves A_{n+1} all eventually cross B_n and C_n . For example, A_{n+1} crosses C_n at $n \simeq 7.1$ and B_n at $n \simeq 9.7$.

we will observe sequentially the three states: Point-Contact, Extended-Contact, and finally Hanging-Fold, before switching to the $n + 1$ mode. In contrast, for $n \geq 8$, we will not observe the Hanging-Fold state and will switch directly from the n th Extended-Contact state to the $n + 1$ th Point-Contact state.

Note that all these arrangements depend on the value of k taken for the number of pieces of the flat region in the Extended-Contact state (here $k = 1$), with $k_{max} = 2n + 1$. In Fig. 14 we plot a high n part of the bifurcation diagram, with $k = 3$, and show the behavior of the system will exhibit multistability and hysteresis. Consider for example that we have loaded the structure by increasing H_Δ/H up to the point U_0 lying at the end of the $k = 3$ segment of the 25th Extended-Contact branch. Upon increasing H_Δ/H further, and if k does not increase, the structure will jump on the point U_1 on the 26th Point-Contact branch. If we then start unloading, the structure will reach point U_2 on the 25th Hanging-Fold branch and, upon further decrease of H_Δ/H , will jump toward on of the points U_3, U_4 , or U_5 . Resuming the loading will close the hysteresis loop.

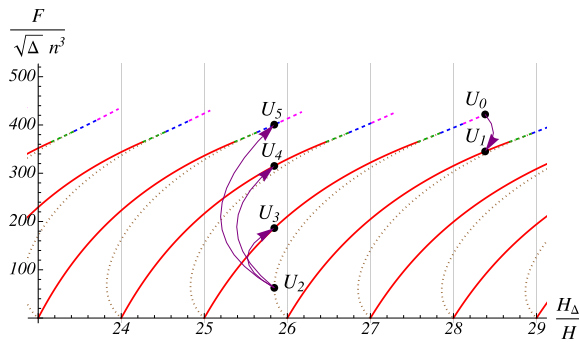


Fig. 14. Hysteresis and multistability at large Atlas number. Starting on point U_1 and decreasing the compaction ratio $H_3/H = (2/\pi)\sqrt{d}/H$ will cause the system to visit point U_2 then jump on either points U_3 , U_4 , or U_5 . Then increasing the compaction ratio will bring the system to U_0 where it will jump on U_1 to close a hysteresis loop. Point-Contact states are plotted as continuous red lines, Extended-Contact states with $k = 1$ as dashed green lines, Extended-Contact states with $k = 2$ as dashed blue lines, Extended-Contact states with $k = 3$ as dashed magenta lines, and Hanging-Fold states as dotted brown lines.

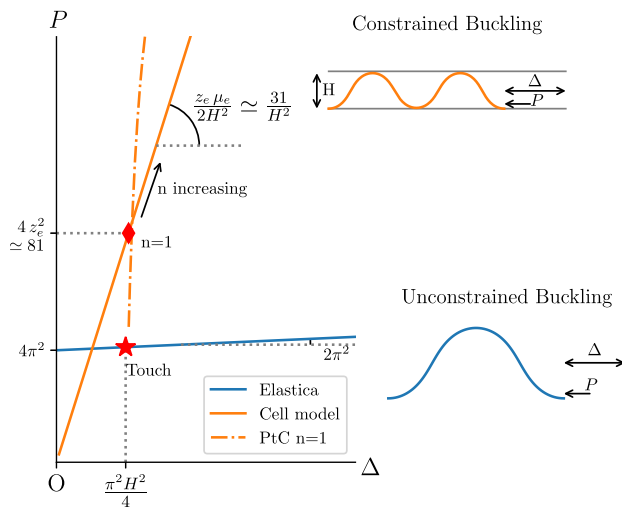


Fig. 15. Buckling an elastica inside a tunnel is much harder than in the unconstrained setup. The horizontal force needed to compress an elastic rod increases much more rapidly in the constrained case (orange) than in the unconstrained case (blue). Note that we have considered the fully nonlinear version of the equilibrium Eqs. (1), (2), (4), (5), (6) for the unconstrained case, where $P(\Delta) = 4\pi^2 + 2\pi^2 \Delta^4$ instead of $P(\Delta) = 4\pi^2$ in the von Kármán approximation, see for example [Bazant and Cedolin \(2010, Fig. 1.26a\)](#).

7. Discussion and conclusion

We have detailed the different equilibrium configurations a planar beam can adopt when buckled in a rectangular cavity (Section 4). We have shown that they are all based on an Arch solution that spans from the lower to the upper wall (Section 3). For each solution type, we have given their range of existence in terms of the imposed horizontal (Δ) and vertical (H) displacements. We have explained how the global system is a repetition of the same solution and have introduced the Atlas number n which counts the repeats. We have used rescaled quantities to illustrate how the vertical (F) and horizontal (P) applied forces vary as functions of the imposed displacements H and Δ , and we have shown that the state of the system during loading is entirely characterized by the compaction ratio $H_{\Delta}/H = (2/\pi)\sqrt{\Delta/H}$. Finally, we have introduced a cellular model that yields an averaged response of the structure as the loads are increased. The cellular model also clearly illustrates why it is much harder to compress and squash a beam inside a cavity than in the unconstrained case, see Fig. 15.

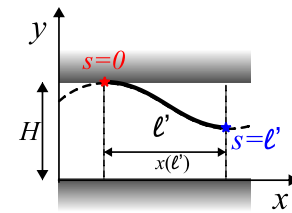


Fig. A.16. Part of the Hanging-fold state in which the beam does not touch both walls.

All the above results are based on the von Kármán kinematic approximation and are then only valid as long as H and Δ are small enough. As $H > 0.2$ and/or $\Delta > 0.1$, the structure enters the full nonlinear regime and, for example, the exact collapse seen in Figs. 7 and 8 is no longer valid, Ying-Yang solutions may appear, and the forces F and P (together with the number n of repeats) will reach maximum values before decreasing (Deboeuf et al., 2024). The global bifurcation diagram, Figs. 12 and 13, gets more complicated and depends on the loading history due to the presence of large hysteresis. These features will be the subject of a subsequent report.

CRediT authorship contribution statement

Jiayu Wang: Writing – review & editing, Writing – original draft, Formal analysis, Conceptualization. **Stéphanie Deboeuf:** Writing – review & editing, Writing – original draft, Formal analysis, Conceptualization. **Arnaud Antkowiak:** Writing – review & editing, Writing – original draft, Formal analysis, Conceptualization. **Sébastien Neukirch:** Writing – review & editing, Writing – original draft, Formal analysis, Conceptualization.

Declaration of competing interest

The authors declare that they have no known competing financial interests or personal relationships that could have appeared to influence the work reported in this paper.

Acknowledgments

The authors gratefully acknowledge the support provided by Sorbonne University and Centre national de la recherche scientifique (CNRS). It is a pleasure to thank Paul Grandgeorge, Eytan Katzav, and Benoit Roman for numerous discussions.

Appendix A. The planar elastica solution in the hanging-fold state

We here compute some basic quantities attached to the Hanging-fold state. In this state, a region of the beam does not touch both walls and its equilibrium is given by a planar elastica solution, see Fig. A.16, with no vertical component in its inner force. We therefore have to integrate system (8) with $n_y(s) \equiv 0$, and the boundary conditions (2a) together with $\theta(\ell') = 0$. The solution of $\theta''(s) = -P \theta(s)$ with $\theta(0) = 0$ is $\theta(s) = c \sin \sqrt{P}s$. Enforcing $\theta(\ell') = 0$ yields

$$\sqrt{P} \ell' = \pi \quad (\text{A.1})$$

Additionally, the continuity of the bending moment at the contact point ($s = 0$ in Fig. A.16) implies that $\theta'(s = 0) = c\sqrt{P}$ equals the value given in Eq. (13). This continuity constraint yields

$$c = \frac{f}{P} \tan \frac{\sqrt{P}\ell}{2} \quad (\text{A.2})$$

Finally, we can compute the horizontal extent of the solution as

$$x(\ell') = \int_0^{\ell'} 1 - (1/2)\theta^2(s) ds = \ell' \left(1 - \frac{c^2}{4} \right) \quad (\text{A.3})$$

Table B.1

Formulas for the forces P and F , the bending energy $2nE_k$, the end shortening Δ , the height H , and the Atlas number n for the cellular model, as functions of different pairs of variables.

	P	F	$2nE_k$	–
(Δ, H)	$31 \frac{\Delta}{H^2}$	$31 \frac{\Delta^2}{H^3}$	$16 \frac{\Delta^2}{H^2}$	$n = 0.62 \frac{\sqrt{\Delta}}{H}$
(Δ, n)	$81 n^2$	$130 n^3 \sqrt{\Delta}$	$40 \Delta n^2$	$H = 0.62 \frac{\sqrt{\Delta}}{n}$
(H, n)	$81 n^2$	$208 H n^4$	$104 H^2 n^4$	$\Delta = 2.6 H^2 n^2$

Appendix B. The cellular model formula in all variables

The solution of the cellular model (Section 5) may be expressed using different pairs of variables. We list in Table B.1 the different possibilities.

Data availability

Data will be made available on request.

References

- Adan, N., Sheinman, I., Altus, E., 1994. Post-buckling behavior of beams under contact constraints. *J. Appl. Mech.* 61, 764–772.
- Bazant, Z.P., Cedolin, L., 2010. *Stability of Structures: Elastic, Inelastic, Fracture, and Damage Theories*. World Science Publishing.
- Bigoni, D., 2012. *Nonlinear Solids Mechanics*. Cambridge University Press.
- Bosten, A., Denoël, V., Cosimo, A., Linn, J., Brüls, O., 2023. A beam contact benchmark with analytic solution. *ZAMM - J. Appl. Math. Mech.* 103 (11), e202200151. <http://dx.doi.org/10.1002/zamm.202200151>.
- Chai, H., 1998. The post-buckling response of a bi-laterally constrained column. *J. Mech. Phys. Solids* 46 (7), 1155–1181. [http://dx.doi.org/10.1016/S0022-5096\(98\)00004-0](http://dx.doi.org/10.1016/S0022-5096(98)00004-0).
- Charrondière, R., Neukirch, S., Bertails-Descoubes, F., 2024. MERCI: Mixed curvature-based elements for computing equilibria of thin elastic ribbons. *ACM Trans. Graph.* 43 (5), art. 160. <http://dx.doi.org/10.1145/3674502>.
- Chateau, X., Nguyen, Q.S., 1991. Buckling of elastic structures in unilateral contact with or without friction. *Eur. J. Mech. A Solids* 10 (1), 71–89.
- Coleman, B.D., Swigon, D., 2004. Theory of self-contact in Kirchhoff rods with applications to supercoiling of knotted and unknotted DNA plasmids. *Philos. Trans. R. Soc. A: Math. Phys. Eng. Sci.* 362, 1281–1299. <http://dx.doi.org/10.1098/rsta.2004.1393>.
- Daviet, G., Bertails-Descoubes, F., Boissieux, L., 2011. A hybrid iterative solver for robustly capturing Coulomb friction in hair dynamics. *ACM Trans. Graph.* 30 (6), art. 139. <http://dx.doi.org/10.1145/2070781.2024173>.
- Deboeuf, S., Protière, S., Katzav, E., 2024. Yin-Yang spiraling transition of a confined buckled elastic sheet. *Phys. Rev. Res.* 6 (1), 013100. <http://dx.doi.org/10.1103/PhysRevResearch.6.013100>.
- Dichmann, D., Li, Y., Maddocks, J., 1996. Hamiltonian formulations and symmetries in rod mechanics. In: Mesirov, J., Schulten, K., Summers, D. (Eds.), *Mathematical Approaches To Biomolecular Structure and Dynamics*. In: The IMA Volumes in Mathematics and Its Applications, vol. 82, Springer Verlag, pp. 71–113. http://dx.doi.org/10.1007/978-1-4612-4066-2_6.
- Djordjorov, P., Vassilev, V., Mladenov, I., 2011. Analytic description and explicit parametrisation of the equilibrium shapes of elastic rings and tubes under uniform hydrostatic pressure. *Int. J. Mech. Sci.* 53 (5), 355–364. <http://dx.doi.org/10.1016/j.ijsmecsci.2011.02.005>.
- Domokos, G., 1994. Global description of elastic bars. *Z. Angew. Math. Mech.* 74 (4), T289–T291. <http://dx.doi.org/10.1002/zamm.19940740410>.
- Domokos, G., Healey, T., 2005. Multiple helical perversions of finite, intrinsically curved rods. *Int. J. Bifurc. Chaos* 15 (3), 871–890. <http://dx.doi.org/10.1142/S0218127405012430>.
- Domokos, G., Holmes, P., Royce, B., 1997. Constrained Euler buckling. *J. Nonlinear Sci.* 7 (3), 281–314. <http://dx.doi.org/10.1007/BF02678090>.
- Eisley, J.G., 1964. Nonlinear vibration of beams and rectangular plates. *Z. Angew. Math. Phys.* (ZAMP) 15 (2), 167–175. <http://dx.doi.org/10.1007/BF01602658>.
- Elettro, H., Neukirch, S., Vollrath, F., Antkowiak, A., 2016. In-drop capillary spooling of spider capture thread inspires hybrid fibers with mixed solid–liquid mechanical properties. *Proc. Natl. Acad. Sci. USA* 113 (22), 6143–6147. <http://dx.doi.org/10.1073/pnas.1602451113>.
- Eringen, A.C., 1952. On the non-linear vibration of elastic bars. *Quart. Appl. Math.* 9 (4), 361–369. <http://dx.doi.org/10.1090/qam/43694>.
- Euler, L., 1744. *Methodus inveniendi lineas curvas maximi minimi propreitate gaudentes*. Opera Omnia I 24, 231–297. URL: <https://scholarlycommons.pacific.edu/euler-works/65/>, Füssli, Zurich 1960.
- Goss, V.G.A., 2009. The history of the planar elastica: Insights into mechanics and scientific method. *Sci. Educ.* 18 (8), 1057–1082. <http://dx.doi.org/10.1007/s11191-008-9166-2>.
- Hearle, J.W.S., 2014. The 20th-century revolution in textile machines and processes. Part 2: Textured yarns and other technologies. *Ind. Archaeol. Rev.* 36 (1), 32–47. <http://dx.doi.org/10.1179/0309072814Z.00000000028>.
- Henderson, M.E., Neukirch, S., 2004. Classification of the spatial clamped elastica: numerical continuation of the solution set. *Int. J. Bifurc. Chaos* 14 (4), 1223–1239. <http://dx.doi.org/10.1142/S0218127404009971>.
- Holmes, P., Domokos, G., Schmitt, J., Szeberényi, I., 1999. Constrained Euler buckling: an interplay of computation and analysis. *Comput. Methods Appl. Mech. Engrg.* 170 (3), 175–207. [http://dx.doi.org/10.1016/S0045-7825\(98\)00194-7](http://dx.doi.org/10.1016/S0045-7825(98)00194-7).
- Judah, N., Givli, S., 2024. The post-buckling behavior of a beam constrained by nonlinear springy walls. *J. Appl. Mech.* 91 (6), 061004. <http://dx.doi.org/10.1115/1.4064684>.
- von Kármán, T., 1907. Festigkeitsprobleme im maschinenbau. In: Klein, F., Müller, C. (Eds.), *Encyklopädie der Mathematischen Wissenschaften*. In: *Mechanik*, Vieweg+Teubner Verlag, Wiesbaden, pp. 311–385. http://dx.doi.org/10.1007/978-3-663-16028-1_5.
- Katz, S., Givli, S., 2015. The post-buckling behavior of a beam constrained by springy walls. *J. Mech. Phys. Solids* 78, 443–466. <http://dx.doi.org/10.1016/j.jmps.2015.02.004>.
- Kehrbaum, S., Maddocks, J.H., 1997. Elastic rods, rigid bodies, quaternions and the last quadrature. *Philos. Trans. R. Soc. Lond. Ser. A, Math. Phys. Sci.* 355 (1732), 2117–2136. <http://dx.doi.org/10.1098/rsta.1997.0113>.
- Kirchhoff, G., 1876. *Vorlesungen über mathematische Physik, Mechanik*. B.G. Teubner, Leipzig. URL: <https://archive.org/details/vorlesungenberm02kirgoog/>.
- Lacarbonara, W., Yabuno, H., 2006. Refined models of elastic beams undergoing large in-plane motions: Theory and experiment. *Int. J. Solids Struct.* 43 (17), 5066–5084. <http://dx.doi.org/10.1016/j.ijsolstr.2005.07.018>.
- Levien, R.L., 2009. *From Spiral to Spline: Optimal Techniques in Interactive Curve Design* (Ph.D. thesis). University of California at Berkeley.
- Love, A.E.H., 1944. *A Treatise on the Mathematical Theory of Elasticity*, fourth ed. Dover Publications, New York.
- Lubinski, A., Althouse, W., 1962. Helical buckling of tubing sealed in packers. *J. Pet. Technol.* 14 (06), 655–670. <http://dx.doi.org/10.2118/178-PA>.
- Manning, R.S., Bulman, G.B., 2005. Stability of an elastic rod buckling into a soft wall. *Proc. R. Soc. A: Math. Phys. Eng. Sci.* 461 (2060), 2423–2450. <http://dx.doi.org/10.1098/rspa.2005.1458>.
- Miller, J., Su, T., Dussan, E., Pabon, J., Wicks, N., Bertoldi, K., Reis, P., 2015. Buckling-induced lock-up of a slender rod injected into a horizontal cylinder. *Int. J. Solids Struct.* 72, 153–164. <http://dx.doi.org/10.1016/j.ijsolstr.2015.07.025>.
- Neukirch, S., Yavari, M., Challamel, N., Thomas, O., 2021. Comparison of the von karman and Kirchhoff models for the post-buckling and vibrations of elastic beams. *J. Theor. Comput. Appl. Mech.* 6828, 1–18. <http://dx.doi.org/10.46298/jtcam.6828>.
- Pandey, A., Moulton, D.E., Vella, D., Holmes, D.P., 2014. Dynamics of snapping beams and jumping poppers. *EPL (Eur. Lett.)* 105 (2), 24001. <http://dx.doi.org/10.1209/0295-5075/105/24001>.
- Pocheau, A., Roman, B., 2004. Uniqueness of solutions for constrained elastica. *Phys. D: Nonlinear Phenom.* 192 (3–4), 161–186. <http://dx.doi.org/10.1016/j.physd.2003.12.013>.
- Roman, B., Pocheau, A., 1999. Buckling cascade of thin plates: Forms, constraints and similarity. *Eur. Lett. (EPL)* 46 (5), 602–608. <http://dx.doi.org/10.1209/epl/i1999-00306-3>.
- Roman, B., Pocheau, A., 2002. Postbuckling of bilaterally constrained rectangular thin plates. *J. Mech. Phys. Solids* 50, 2379–2401. [http://dx.doi.org/10.1016/S0022-5096\(02\)00028-5](http://dx.doi.org/10.1016/S0022-5096(02)00028-5).
- Schulz, M., Pellegrino, S., 2000. Equilibrium paths of mechanical systems with unilateral constraints. I. Theory. *Proc. R. Soc. A: Math. Phys. Eng. Sci.* 456 (2001), 2223–2242. <http://dx.doi.org/10.1098/rspa.2000.0611>.
- Thomas, O., 2025. Understanding, computing and identifying the nonlinear dynamics of elastic and piezoelectric structures thanks to nonlinear modes. In: *Model Order Reduction for Design, Analysis and Control of Nonlinear Vibratory Systems*. In: Series CISM courses and lectures, vol. 614, Springer, pp. 151–236. http://dx.doi.org/10.1007/978-3-031-67499-0_4.
- Thomas, O., Sénéchal, A., Deü, J.-F., 2016. Hardening/softening behavior and reduced order modeling of nonlinear vibrations of rotating cantilever beams. *Nonlinear Dynam.* 86 (2), 1293–1318. <http://dx.doi.org/10.1007/s11071-016-2965-0>.
- Thomson, W., Tait, P.G., 1883. *Treatise on Natural Philosophy*, vol. 2, Cambridge University Press.
- Tzokova, P.S., 2020. *Confined Wrinkling of Thin Elastic Rods, Sheets and Cones* (Ph.D. thesis). University of Cambridge, <http://dx.doi.org/10.17863/CAM.57977>.
- Vetter, R., Wittel, F.K., Herrmann, H.J., 2014. Morphogenesis of filaments growing in flexible confinements. *Nat. Commun.* 5, 4437. <http://dx.doi.org/10.1038/ncomms5437>.

- Villaggio, P., 1979. Buckling under unilateral constraints. *Int. J. Solids Struct.* 15 (3), 193–201. [http://dx.doi.org/10.1016/0020-7683\(79\)90030-1](http://dx.doi.org/10.1016/0020-7683(79)90030-1).
- Wachter, A., Biegler, L.T., 2006. On the implementation of an interior-point filter line-search algorithm for large-scale nonlinear programming. *Math. Program. Ser. A* 106, 25–57. <http://dx.doi.org/10.1007/s10107-004-0559-y>.
- Wang, J., Deboeuf, S., Antkowiak, A., Neukirch, S., 2025. Constrained Euler Buckling: Global Nonlinear Phase Diagram. Technical Report, Sorbonne University.
- Woinowsky-Krieger, S., 1950. The effect of an axial force on the vibration of hinged bars. *J. Appl. Mech.* 17, 35–36, URL: <https://hal.science/hal-03184616>.